doi:10.26443/seismica.v5i2.2551

SEISMICA

Seismo-Acoustic Meteoroid Observation Recording Database (SMORD): A Global Dataset and Deep-Learning Phase Picker for Meteoroid-Generated Air-to-Ground Coupled Seismic Waves

Dario Eickhoff *[1], **Runa Ostermeier** [1], **Joachim Ritter** [1]

[1]Karlsruhe Institute of Technology, Geophysical Institute, Karlsruhe, Germany

Author contributions: *Conceptualization*: D. Eickhoff, J. Ritter. *Data Curation*: D. Eickhoff, R. Ostermeier. *Formal Analysis*: D. Eickhoff. *Funding Acquisition*: J. Ritter. *Investigation*: D. Eickhoff, R. Ostermeier. *Methodology*: D. Eickhoff. *Project Administration*: J. Ritter. *Resources*: J. Ritter. *Software*: D. Eickhoff. *Supervision*: J. Ritter. *Validation*: D. Eickhoff. *Visualization*: D. Eickhoff. *Writing – original draft*: D. Eickhoff. *Writing – review & editing*: D. Eickhoff, R. Ostermeier, J. Ritter.

Abstract Meteoroids impacting Earth's atmosphere generate acoustic waves that can couple into the ground and can be recorded by dense, globally distributed seismic networks. Thus, these records complement optical and radar observations, especially since seismic stations also operate in cloudy weather conditions and during daytime. However, open datasets that link meteoroid events to labeled seismic waveforms are scarce, limiting the development of automated detectors for meteoroid-induced seismo-acoustic signals. We introduce the **S**eismo-acoustic **M**eteoroid **O**bservation **R**ecording **D**atabase (SMORD), compiled by cross-referencing public meteoroid catalogs (International Meteor Organization fireball reports; NASA CNEOS fireball catalog) with seismic archives. Continuous waveforms are manually labeled for the first clear meteoroid-related onset of air-to-ground coupled seismic waves using a three-level pick-quality scheme. SMORD v1.0 contains 310 meteoroid events and 3,295 labeled arrivals across a global station set. Using SMORD labels, we train a PhaseNet picker in SeisBench with station-level splits and augmentation. On test data, the model achieves 91% precision and 94% recall at a 0.5 decision threshold (area-under-curve value 0.89), with median absolute timing error of 0.02 s (90% within c. $\pm$0.3 s). We demonstrate automated onset detection and trajectory reconstruction for an April 2025 Adriatic fireball, highlighting the values of SMORD for rapid post-event analysis.

Production Editor:
Yen Joe Tan
Handling Editor:
Kenneth Macpherson
Copy & Layout Editor:
Hannah F. Mark

Signed reviewer(s):
Christoph Pilger

Received:
January 26, 2026
Accepted:
May 6, 2026
Published:
July 3, 2026

Non-technical summary When a bright meteor, or fireball, enters the Earth's atmosphere, it generates a powerful acoustic wave in the air. This wave can shake the ground slightly, and sensitive earthquake-monitoring stations can detect it. Since these stations operate day and night and are unaffected by clouds, they can detect fireballs even when camera systems or radars miss them.However, the lack of a well-organized, shared collection of these fireball signals in seismic data is a major challenge. To address this, we created a **S**eismo-acoustic **M**eteoroid **O**bservation **R**ecording **D**atabase (SMORD). SMORD is an open database that links reported fireball events from public sources with the corresponding seismic recordings from nearby earthquake stations. We gathered relevant seismic recordings and marked the first onset time of each fireball signal, which can be used to calculate their trajectories.SMORD currently includes 310 fireball events and 3,295 marked signal arrivals from seismic stations worldwide. Using these examples, we train a machine-learning tool that can identify fireball-related signals in new seismic data with high reliability and precise timing. We demonstrate how this tool can quickly detect a fireball and estimate its travel path through the atmosphere, supporting rapid follow-up studies after an event.

1 Introduction

Earth is constantly subjected to an influx of interplanetary matter and most of this mass arrives as interplanetary dust (Drolshagen et al., 2017). As the size and mass of this matter increases, penetration depth into Earth's atmosphere increases as well (e.g., Gritsevich, 2009). Surpassing 30 μm these objects are classified as meteoroids (Koschny and Borovicka, 2017). Meteoroids impacting Earth are studied by different techniques: optical observations by ground-based camera networks (e.g., FRIPON, see Colas et al., 2020), space-based optical detections (e.g., the GOES Geostationary Lightning Mapper (GLM), see Jenniskens et al., 2018), reports from human observers (e.g., IMO Fireball Program, see Hankey and Perlerin, 2014; International Meteor Organization, 2025a), radio forward-scatter and radar systems (e.g., CMOR, see Webster et al., 2004; Jones et al., 2005; BRAMS see, Lamy et al., 2023), infrasound measurements (e.g., Ens et al., 2012; Ott et al., 2019; Pilger et al., 2020; Silber, 2024), and seismo-acoustic methods that

*Corresponding author: dario.eickhoff@kit.edu

track ground-coupled airwaves at seismic stations (e.g., ReVelle, 1976; Edwards et al., 2008; Neidhart et al., 2021).

Optical and radio techniques rely on ionization produced along the meteoroid trail, whereas seismo-acoustic methods are based on the shock wave induced by a meteoroid while it travels at supersonic speed. Atmospheric entry speeds of meteoroids range from about 11 km s^{-1} to 72 km s^{-1} (Ceplecha et al., 1998; Moorhead et al., 2019), considerably exceeding the velocity of sound in the atmosphere (c. 290–350 m s^{-1}). After coupling into the solid Earth, seismic waves are excited with much higher propagation velocities compared to the velocity of sound, while still being significantly slower than the meteoroids themselves. In Fig. 1, three events with recording examples of meteoroid-induced signals are presented.

A key advantage of seismo-acoustic observations is the abundance and global distribution of seismic sensors, which provide broad and dense spatial coverage compared with the much smaller number of dedicated meteor cameras. These cameras, in turn, greatly outnumber meteor radar systems (e.g., Andrioli et al., 2013; Vida et al., 2021; Ringler et al., 2022). Additionally, seismo-acoustic stations are independent of cloud coverage and light conditions, which especially inhibit optical detections. Previous studies have demonstrated that meteoroids produce infrasound that can be readily detected (ReVelle, 1976; Silber et al., 2015) and that a portion of this acoustic energy couples into the ground and can be recorded with seismic instruments (Edwards et al., 2007, 2008; Novoselov et al., 2020). Observational studies have shown that infrasound sensors can reliably detect acoustic waves from meteoroids with masses ranging from grams to tens of kilograms (Silber and Brown, 2014). Seismic stations, however, record ground motions that have undergone acoustic-to-seismic or air-to-ground coupling in the case of meteoroid signals. In this study, we focus on the so-called direct coupled airwave (e.g., Edwards et al., 2008) that produces characteristic W-shaped wavelets on seismic recordings, because they are easy to identify and exhibit the best signal-to-noise ratios. They are called direct coupled airwaves because the coupling into the ground happens close to the seismometer. Estimates of acoustic-to-seismic coupling efficiency commonly lie in the ~1–3 % range (Novoselov et al., 2020); this variability is closely linked to near-surface site conditions, such as the stiffness of the local geological material and other surface conditions, e.g., topography (Edwards et al., 2008; Novoselov et al., 2020). Another factor is the incidence angle of the meteoroid: steeply incident meteoroids radiate acoustic waves nearly parallel to the Earth's surface and, therefore, are harder to detect (Neidhart et al., 2021). Neidhart et al. (2021) identified meteoroid related signals on seismic sensors for meteoroid masses ranging from 1 g to 10^5 g. Their study determines a lower limit of meteoroid masses that can be recorded with seismometers. It shows that the lower mass end of recordable meteoroids is well below 10^3 g, which is the order of magnitude at which larger meteoroids begin to pose potential hazards at Earth's surface, highlighting the importance of rapid and reliable detection. Thus, seismological studies can contribute to quantifying the meteoroid flux to assess risks associated with these extraterrestrial bodies. In addition, a rapid calculation of the trajectory, which is the path the meteoroid takes through the atmosphere, can help to recover the extraterrestrial material for further studies. Meteoroid trajectories have been reconstructed by seismo-acoustic signals before (e.g., Arrowsmith et al., 2007; Vera Rodriguez et al., 2022) and there exist geometrical reconstruction methods (e.g., Pujol et al., 2005), as well as ray-based approaches that can include the effects of atmospheric winds (e.g., Blom et al., 2024).

For these reasons, we focus on meteoroid events from publicly accessible catalogs which contain significant events: the International Meteor Organization (IMO) fireball event lists derived from crowd-sourced visual human observer reports (International Meteor Organization, 2025a) and the NASA Center for Near-Earth Object Studies (CNEOS) fireball catalog compiled from U.S. Government sensors (NASA/JPL, 2025).

Open datasets linking meteoroid events to seismic waveforms and arrival onsets remain scarce, and automated detectors trained specifically on meteoroid-generated signals do not exist yet or are unknown to the authors. Therefore, we introduce the Seismo-acoustic Meteoroid Observation Recording Database (SMORD), compiled from cross-referencing public meteor event catalogs with regional seismic observations and by manually labeling meteoroid-related phase arrivals. We describe the database, data sources, and labeling protocol. Furthermore, we develop and evaluate a phase-arrival picker based on PhaseNet via SeisBench (Zhu and Beroza, 2019; Woollam et al., 2022) trained on SMORD labels. We report accuracy, precision, and recall on test data, which was not part of the training. Finally, we demonstrate automatic phase detection for meteoroid acoustic-to-seismic signals and trajectory reconstruction using SMORD, as well as its current limitations.

2 Data

2.1 Meteoroid event catalogs

IMO Fireball Program: The event catalog of the IMO fireball program is a community-driven, publicly browsable database of fireball events reported by human observers (Hankey and Perlerin, 2014). For our selection we restrict IMO events to those with $\geq$100 independent reports to prioritize well-constrained trajectories. We analyze all IMO events from 2010–2023 and selected events from 2024. Because the database relies on human witnesses, the events cluster near population centers and during times of day when many people are awake. For each IMO event, we take the reported trajectory beginning and end points and calculate the midpoint along the trajectory. Then we search for seismic stations within a great-circle distance of 3° from this midpoint. The catalog also includes six re-entry events of space debris, which produce seismo-acoustic signals analogous to meteoroids (e.g., Fernando and Charalambous, 2026; Fernando et al., 2024); these are included in

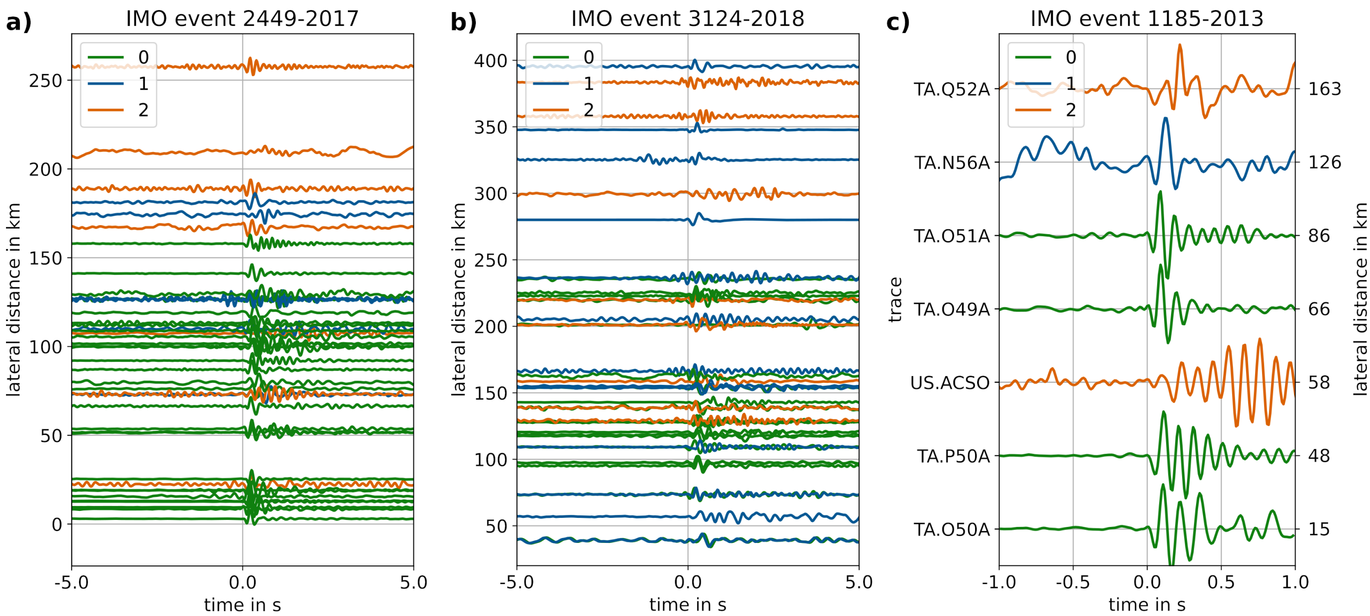

Figure 1 Vertical component waveform examples of meteoroid signals. Lateral distance is relative to the center of the trajectory, and time zero corresponds to the onset time of each signal arrival which is manually picked. The waveforms are colored with respect to the pick quality (0/green: high pick quality, 1/blue: moderate pick quality, 2/orange: low pick quality, see Table 1). Here seismo-acoustic onsets can be identified at lateral distances of a) up to 260 km for an event above Washington State and b) up to 390 km for an event above Italy. c) Detailed view of waveform examples for the different pick qualities for the IMO event 1185-2013 over Ohio State. The Y-axis annotations represent the network-station-code combination (FDSN) for each seismogram. Time (along the X-axis) is relative to picked onset time. The waveforms are bandpass filtered from 1–10 Hz and the traces are normalized.

SMORD but flagged for optional filtering.

CNEOS fireball catalog: We use all CNEOS events compiled by NASA/JPL (NASA/JPL, 2025) from 1988-2024 with reported estimated yields $\geq$0.3 kt TNT equivalent to prioritize energetic airbursts expected to radiate strong acoustic waves. The CNEOS events are based on U.S. Government space-based sensors and provide a near-global coverage. As with IMO, we take the reported event location, but we increase the search radius for seismic stations to 5° to reflect (1) weaker ties of CNEOS detections to population centers and dense seismic networks, and (2) generally higher signal-to-noise (SNR) ratios for higher-yield events.

2.2 Waveform retrieval and preprocessing

Continuous waveforms are downloaded using public FDSN services (e.g., the EIDA Federator, see Strollo et al., 2021; the IRIS DMC, see Trabant et al., 2012; the NCEDC, see Northern California Earthquake Data Center, 2014; the SCEDC, see SCEDC, 2013; Raspberry Shake, see Raspberry Shake, S. A., 2016) with ObsPy (Beyreuther et al., 2010). Network, station, location, and channel codes are stored in SMORD. Preprocessing for picking includes instrument-response removal (to ground velocity), detrending, and band-pass filtering (varied in the frequency band 0.5–40 Hz) to emphasize the onsets of the acoustic-to-seismic signals. Time windows are aligned relative to catalog event times with padding to accommodate atmospheric propagation delays and catalog uncertainties in location and origin time.

3 Methods

3.1 Manual phase picking and labeling protocol

We visually inspect time windows around expected wave arrivals at each recording station and manually pick the first clear onset attributed to the meteoroid-related wave. The time windows are selected around the arrival time of an acoustic wave traveling with 330 m/s with the time window width increasing with increasing origin-station distance. The time windows are additionally expanded in both directions by 120 s to account for the uncertainty of the vertical location of the meteoroid source. Selection criteria include an impulsive, negative-polarity onset on the vertical component, with a dominant frequency between 1–20 Hz, consistent with ground-coupled airwaves (i.e., W-shaped wavelets; see Edwards et al., 2008). For further verification, we check for a plausible moveout of an acoustic wave, cross-component coherence, and exclusion of disturbing local anthropogenic or tectonic phase arrivals. Each pick receives a quality flag of 0 to 2 (best to worst) that is chosen depending on onset clarity and signal-to-noise ratio (SNR) (see Figure 1c; Table 1). In the case of onsets with characteristics of two different qualities, e.g., a clear onset with only moderate amplitude, the resulting pick quality will be the lower one of the two quality identifiers; in this exemplary case a pick quality of 1 would be attributed.

Metadata are stored per pick with including event and station identifiers as well as locations. Picks have an associated pick time in UTC, network/station/location code, channel, and quality flag (see Table 2).

3.2 Model training with SeisBench PhaseNet

To automatically find seismic signals of meteoroids, we trained a probabilistic seismic phase picker using PhaseNet (Zhu and Beroza, 2019), as implemented in the SeisBench framework (Woollam et al., 2022). SeisBench provides standardized access to waveform datasets, preprocessing routines, and benchmark models for seismological machine learning (Woollam et al., 2022). PhaseNet is a deep convolutional neural network that maps multi-component waveform windows to phase-probability time series (Zhu and Beroza, 2019). This routine makes it well-suited for robust P- and S-phase picking in noisy environments. In our setup, we train the network on positive windows centered on analyst labeled arrivals, off-center positive windows, and negative windows. Training proceeds over multiple epochs, during which the model updates its parameters iteratively to minimize a weighted cross-entropy loss that encourages sharp phase probability estimates. This strategy leverages the strengths of neural networks to learn complex nonlinear relationships in seismic data while controlling overfitting through data augmentation and repeated exposure to diverse positive examples.

SMORD waveforms and labels are packaged as a SeisBench WaveformDataset (Münchmeyer and Woollam, 2025; Woollam et al., 2022). For training, the raw, unprocessed time series are resampled to a common 100 Hz sampling rate, which is consistent with the standard configuration of PhaseNet (Zhu and Beroza, 2019). The dataset is partitioned into disjoint training, development, and test subsets with an 80/10/10 split at the station level. This ensures that all waveform windows derived from a given station across all meteoroid events appear in only one subset. This grouping prevents train-to-test contamination, i.e., data leakage, in which nearly identical waveform segments would be present in both the training and evaluation data. Contamination would lead to overly optimistic validation performance and poor generalization (Sasse et al., 2025), which is mitigated by our strategy.

Since meteoroid events are usually observed at multiple stations, the station-level split allows each subset to sample a variety of events while keeping station-specific effects separate. This better reflects the intended application to unseen stations and follows common machine learning practice for grouped or correlated data, where samples sharing a common identifier are kept within the same split to obtain an unbiased estimate of model performance (Sasse et al., 2025).

To train the network, we use three different complementary generators that let the network learn the pattern of wave onsets, while being robust to different source-receiver orientations and noise:

1) positive windows centered on labeled meteoroid signal onsets,

2) augmented positive windows which are identical to 1 but with on-the-fly data augmentation: random rotations in the horizontal plane and additive Gaussian noise, and

3) noise-only windows drawn uniformly from training records and explicitly labeled as “N” (noise) to control false positives.

The first generator allows the network to learn the typical waveform patterns associated with arrivals of meteoroid signals, e.g., onset shape, polarity, and relative timing between components. Using 1) as a distinct generator ensures that enough genuine onsets are contained in every batch, so that the model can learn a sharp phase likelihood for true arrivals. The second generator uses the same positive samples but with random horizontal component rotations that simulate different source-receiver geometries. The additive Gaussian noise used in this generator teaches the network to keep detecting onsets even as the SNR diminishes. Because these augmentations are re-applied during each epoch, the model effectively sees a much larger variety of examples, which reduces overfitting and improves generalization. The third generator teaches the network to identify noise, which reduces false positives.

The three generators are concatenated to form the training stream used by PyTorch (Paszke et al., 2019) and increase the amount of training data for each epoch. In this way the data is increased from 2,637 signals for only generator 1 to over 7,911 signals with all three generators. Time windows are 6,000 samples long (60 s at 100 Hz), with the labeled onset randomly positioned within the window followed by a zero padding to maintain fixed length across all windows.

We train a PhaseNet architecture from SeisBench configured for three per-sample classes P/S/N (with S unused here) from scratch, because meteoroid air-to-ground coupled phases differ fundamentally from earthquake P- and S-phases and no suitable pre-trained models exist for this signal class. Inputs are three-component seismograms (Z, N, E) if available, otherwise vertical (Z) recordings only. To encourage orientation invariance, we apply random rotations in the horizontal plane, and to simulate a variable noise floor we add Gaussian noise which scales up to ~10 % of the normalized amplitude for each epoch for generator 2. All inputs are demeaned and peak-normalized within the window.

Labels are produced as probabilistic time series with a Gaussian smoothing across 20 samples (0.2 s at 100 Hz). For positive examples, we use the single manually picked meteoroid signal onset and map it to the P-wave channel (the S-wave channel remains unused, as there are no labelled S-phase picks associated with acoustic meteoroid-induced seismic waves; no S-phases are contained in SMORD). Noise-only windows are labeled N = 1 everywhere. The network thus learns a per-sample posterior over P/S/N tailored to meteoroid air-to-ground coupled seismic wave onsets.

We use the AdamW optimizer from PyTorch (Paszke et al., 2019) with a learning rate of 10^{-3} and a weight decay of 10^{-2}. These are unitless hyperparameters that control update magnitude and regularization strength,

Pick quality	High (0)	Moderate (1)	Low (2)
onset clarity (I)	clear W-shaped wavelet	slightly distorted or wavelet with multiple peaks/troughs	wavelet with multiple peaks/troughs or no clear onset; emergent waveforms
SNR (II)	W amplitude is elevated significantly above the noise	W amplitude is elevated moderately above the noise	W amplitude is close to the noise

Table 1 Guidelines for decision-making for pick quality.

Metadata type	Value
Event id	IMO 1185-2013
Event origin time	2013-05-31T03:03:00.000
Event location	40.014 °N; 83.598 °W
Station network code	TA
Station code	O94A
Trace channels	BH*
Trace sampling rate	40 Hz
Station location	40.188 °N; 84.335 °W; 292 m
Phase pick quality	0
Trace start time	2013-05-31T03:06:46.000
P phase arrival sample	4006
Split	Train

Table 2 Metadata of a phase pick stored in SMORD with exemplary values. The P phase arrival sample marks the waveform sample at which the meteoroid related onset is picked. The split, either train, dev, or test is the separation of the dataset into the three groups used for the PhaseNet training (see Section 3.2).

respectively. The AdamW optimizer combines adaptive step sizes, or per-parameter learning rates based on running estimates of gradient mean and variance, with decoupled weight decay. This improves the behavior of weight decay for adaptive optimizers compared to classic L2-penalty formulations (Loshchilov and Hutter, 2017). We use cosine annealing to schedule the learning rate across 500 epochs, yielding large updates early on and progressively smaller updates later on for fine-tuning (Loshchilov and Hutter, 2016). To stabilize optimization, we apply global gradient-norm clipping with an L2-norm threshold of 1.0. This means that if the overall L2-norm of the gradients across all parameters exceeds 1.0, the gradients are rescaled to prevent excessively large parameter updates that could destabilize the training (Pascanu et al., 2013). For each time sample, the model outputs softmax probabilities for the P/S/N classes (e.g., Bridle, 1990). We train with class-weighted cross-entropy (weights of 1.0, 0.0, and 0.4 for P, S, and N, respectively) and then average the loss over all time samples and across the batch. Class weighting is a standard approach for imbalanced classes (i.e., the P and N classes in this case) and per-sample supervision (Buda et al., 2018). We monitor the loss for each epoch on the development split of the dataset, and we save the model with the best loss.

4 Results

SMORD currently contains 310 distinct meteoroid and 6 re-entry events as well as 3,295 labeled seismo-acoustic picks across a global station set of 1,772 seismological recording stations (SMORD v1.0). Of the 316 events, 262 are taken from the IMO Fireball event list (~83 %), accounting for 3,083 associated picks (~94 %). CNEOS events represent ~17 % of the database and they contribute to ~6 % of labeled picks. The contribution of picks from the CNEOS database is lower, because events can be identified over the open ocean far away from seismometers. Here, we only include the events where we identified at least one meteoroid-related phase. Events cluster around densely populated regions of central Europe and the eastern United States (Fig. 2), a consequence of the eyewitness-driven IMO contribution. We partly mitigated this bias by including the CNEOS list, which is less location- and time-biased. Thereby events are added from the southern hemisphere as well.

Of the 310 meteoroid events, 218 occurred in North America, 61 in Europe, and 31 elsewhere. Only 18 events were reported from the southern hemisphere. Figure 3 summarizes key features of SMORD metadata. Before 2010, only CNEOS events are included in SMORD, because no IMO events reached the threshold of $\geq$100 observers. The CNEOS list provides on average one event per year to SMORD. After 2010, as the IMO program grew, the number of SMORD events per year rose markedly. Figures 3b-c show the event-

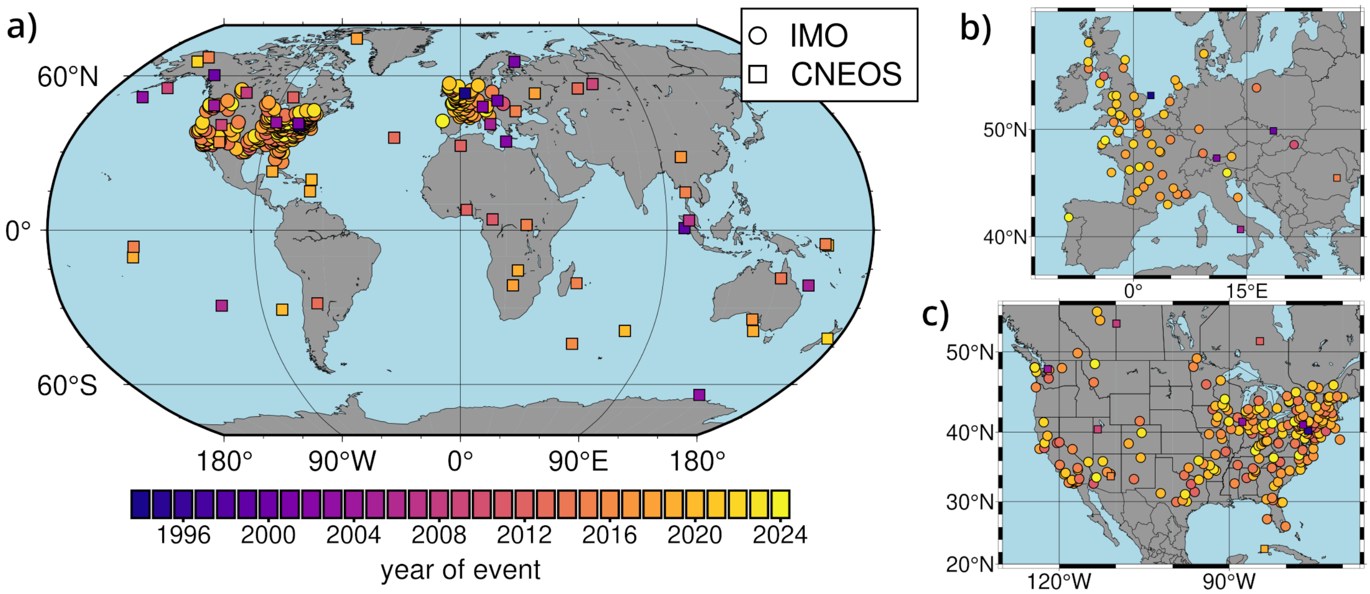

Figure 2 a) World map of SMORD events. Colored circles mark IMO (International Meteor Organization, 2025a) events and colored squares mark CNEOS (NASA/JPL, 2025) events. Events are colored with respect to the year of their respective occurrence. The same coloring and marking are used in b) and c). b) Zoomed-in map with Central European events. c) Zoomed-in map with North American events.

time distribution over UTC and local time. The high number of events at 0 – 4 h UTC time coincides with evening to night times in North America and Western Europe, respectively, which indicates the diurnal bias of the dataset. This bias becomes much clearer when the event times are given in local times for the event locations (see Fig 3c). There, the paucity of 0 – 6 h local-time events (Fig. 3c) reflects the eyewitness nature of IMO events, as at this time most people are asleep. Observational studies indicate that meteoroid flux at night is approximately uniform with enhancements near dusk and dawn (e.g., Brown et al., 2007; Silber et al., 2015). This means that SMORD is currently heavily biased towards human wake-sleep cycles as near-dusk events are mostly well represented, but near-dawn events are underrepresented.

Figure 3d shows the temporal distribution of SMORD meteoroid events by month and year. About two-thirds of all detections occur between October and February. This pattern aligns with the longer winter nights in the Northern Hemisphere, which increase the likelihood of observing meteoroid events. In contrast, August shows an unusually low number of detections even though the Perseid meteor shower peaks in that month. We interpret this as an indication that most SMORD events do not arise from dedicated meteor-observing campaigns scheduled around major showers. Instead, events are observed opportunistically when observers are awake and conditions are favorable. In such a scenario, the shorter nights and increased daylight in August naturally lead to fewer sightings, resulting in the comparatively weak representation of Perseid activity in our sample. However, due to the uncertainties in the IMO and CNEOS trajectories, the meteoroids in the SMORD database are not associated with meteor showers.

The distribution of the number of individual phase picks against the lateral distance from the center of the meteoroid trajectory is given in Fig. 3e. Because event heights are not uniformly reported in the IMO and CNEOS catalogs, we opt to consider only the lateral distance, meaning we ignore height information in the distance calculation. Instead, we calculate distance using the horizontal offset to the trajectory midpoint.

The number of phase picks decreases with increasing station range with a peak at a lateral station-event distance distinct for each quality: this peak is around 80 km distance for the good (0) quality picks. The medium quality (1) peaks at a lateral distance of c. 140 km, while the phase picks of poor (2) quality peak at a lateral distance of c. 160 km.

The offset of the peak in number of phase picks relative to 0 km lateral distance at the center of the trajectory may result from limitations in the distance definition and altitude-dependent source strength (see Figure 3e). This projection may shift the apparent location picks relative to the midpoint. Additionally, acoustic emissions produced during the latter stages of flight at lower altitudes are expected to yield higher signal-to-noise ratios at the seismic stations, which increases the likelihood of confident detections (e.g., Silber and Bowman, 2025). However, signals from meteoroid fragmentation cannot easily be discriminated from signals due to Mach cone waves, based only on individual waveforms. Instead a source determination is required to discriminate between the underlaying point or line source. The observed clustering of picks at ~80 – 160 km distance is consistent with a combination of geometric bias and enhanced detectability of signals from the lower portion of the trajectory. The decrease of phase picks with distance aligns with the expected decrease in SNR over greater distances and thus also increasing travel times (Fig. 3e).

Across all events, the median number of picked arrival phases per event is 7.5 (Fig. 3f). The values in

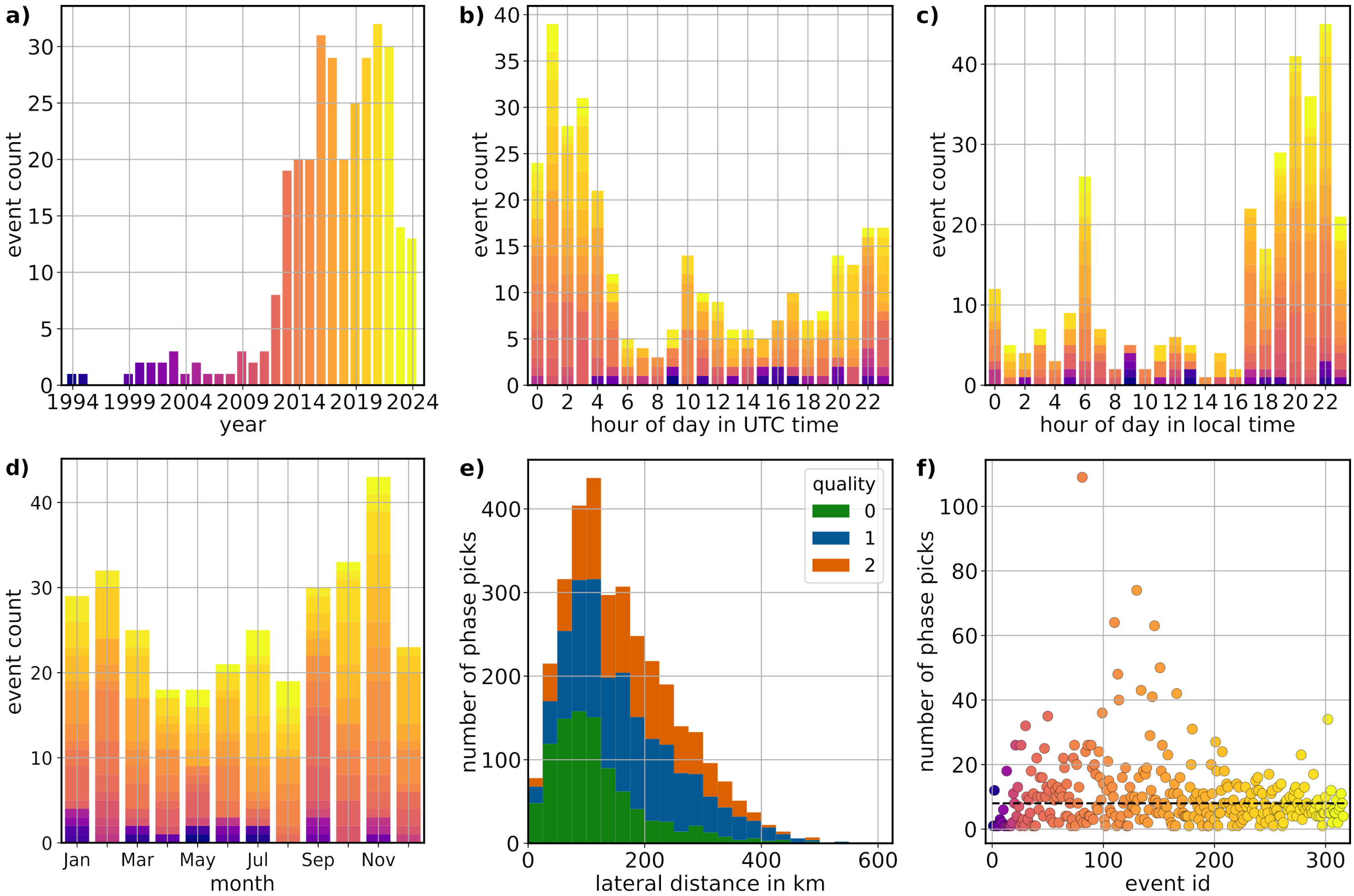

Figure 3 Statistics of SMORD metadata. a) Count of meteoroid events (at least one picked seismic arrival exists) versus year of the event. Purple to yellow coloring is the same as in Figure 2 and Figs. 3b, 3c, 3d, 3f. b) Count of meteoroid events versus UTC event time. c) Count of meteoroid events versus local event time. d) Count of meteoroids versus month of the event. e) Count of individual phase picks versus their lateral distance from the trajectory midpoint. The coloring indicates the quality of the individual phase pick from 0 (best/good) to 2 (worst/poor). f) Number of overall phase picks versus individual event id. The dashed black line represents the median phase pick number of 7.5 picks per event.

Fig. 3f are stable over time, with outliers for large bolides over dense seismic networks which, of course, produce more signals with high amplitudes, e.g., event id 81 (IMO 2015-657; 109 picks, event above Switzerland) and id 130 (IMO 2017-1298; 74 picks, event above California).

We evaluate the performance of the PhaseNet-based picker (hereafter PN picker) using standard binary-classification metrics derived from the entries of the confusion matrix, following e.g., Sokolova and Lapalme (2009), with true positives (TP), false positives (FP), true negatives (TN), and false negatives (FN), which are computed by comparing predicted onset detections to the manually picked reference labels. Because the PN picker outputs a probability for the presence of a seismo-acoustic onset, a fixed probability decision threshold τ is used to convert probabilities into binary predictions (i.e., onset vs no onset). We measure overall performance of the PN picker at this fixed τ with the metrics given in Table 3.

With the test subset, the PN picker achieved 91% precision and 94% recall for identifying seismo-acoustic meteoroid signal onsets for a fixed decision threshold of 0.5 (see Figure 4a) that was selected on the development subset. An AUC value of 0.89 (see Figure 4b) indicates a discriminative power that is well above the 0.5 chance level of a random picker. The AUC value is calculated by first calculating the receiver operating characteristic (ROC) over a range of decision thresholds. The ROC is calculated by comparing the true positive rate with the false positive rate. The true positive rate indicates the proportion of positive cases that are correctly identified as such, while the false positive rate indicates the proportion of negative cases that are incorrectly classified as positive. The high AUC value implies that, operationally, we can raise or lower the decision threshold to prioritize fewer false alarms or fewer misses without collapsing the performance. Pick timing uncertainty as displayed in Figure 4c is likewise robust over the test subset and different meteoroid events. Picking uncertainties cluster tightly around zero with a median absolute uncertainty of 0.02 s and with 90% of the uncertainties between -0.31 s and +0.29 s. These uncertainty values are quite low for inverting source parameters, because wave propagation is applied in a low-velocity acoustic medium (290–350 m/s), quite different from solid Earth situations with higher seismic velocities. Figure 4d shows a comparison between the manually picked onsets (blue) and PN predicted probability distributions (red) as a record section over a random as-

Metric	Formula	Measure
precision	$\frac{TP}{TP+FP}$	fraction of correctly predicted onsets
recall	$\frac{TP}{TP+FN}$	fraction of correctly detected true onsets
F1 score	$\frac{Precision \cdot Recall}{Precision+Recall}$	balance between precision and recall
AUC (area under the curve)	$\frac{1}{2}\left(Recall+\frac{TN}{TN+FP}\right)$	threshold independent discrimination ability between positives and negatives

Table 3 PN picker performance metrics (modified after Sokolova and Lapalme, 2009). TP: true positives, FP: false positives, TN: true negatives, FN: false negatives.

sortment of traces. These visual comparisons as well as the performance metrics and timing uncertainty of the PN picks confirm that the trained model not only separates signal from noise reliably but also localizes the time onset to within a few tenths of a second with a success rate of roughly 90% over all phase picks.

The performance of the PN picker is robust for a large lateral distance range (Fig. 5), and we do not find a performance degradation directly related to increased distance ranges, which could be expected as the SNR generally decreases with distance (Fig. 5a).

PN picks with an increased pick uncertainty (>|0.5| s) do not seem to cluster either at large lateral distances or for low SNR signals, while pick probability correlates with pick uncertainty. In Figure 5b picks with a higher uncertainty do not cluster below a specific SNR and seem to be erratically distributed with distance to the source.

5 Application

The picked arrival times can be used to calculate the meteoroid trajectory, which is important to estimate the possible strewn field on Earth's surface or the meteor origin in space. Here, we present an application to the fireball event listed as IMO Event 2025-2077 (International Meteor Organization, 2025b) and FRIPON Event 24644 (Fireball Recovery and InterPlanetary Observation Nework, 2025). This fireball crossed the Adriatic Sea coming from Southeastern Europe towards Northern Italy on 12th April 2025 at 18:58 UTC. IMO received 401 reports from visual observations and the FRIPON camera network had 12 recordings. These data sources are used for a comparison with our trajectory solutions (Table 4).

The following 4-step workflow is applied:

1. Download of seismic waveform data for recording stations within 2.5° distance around the average midpoint between the FRIPON and IMO of 45°N, 13.5°E.
2. Prediction of onset times automatically with the PN picker using time padding around the modeled acoustic travel time from the reported trajectory to each station.
3. Calculation of 100 bootstrapped fast trajectory fits using particle swarm optimization (PSO) (e.g., Kennedy and Eberhart, 1995; Miranda, 2018), based solely on a random subset of 80 percent of PN picks at a fixed decision threshold of 0.3, 0.4, and 0.5.
4. Repetition of step 3 after a manual screen of the PN picked subset of waveforms and adjusting two outlier picks (seismic stations PE3 and SSFR).

As there are two outliers in the data, we call case 1 the one without correction (Fig. 6a, c, e) and case 2 the other one for which we checked the picks and corrected the two pick times manually (Fig. 6b, d, f). The solutions at decision threshold $\tau = 0.3$ for cases 1 and 2 result in a substantially wider spread of solutions over the 100 bootstrapped runs at 80 per cent of the amount of PN picks compared to the solutions at higher thresholds. The two manually corrected picks significantly improve the model fit based on the RMSE measured as difference of measured and modelled arrival times. Based on that, we find the best fitting solution for $\tau = 0.4$ with an RMSE of 2.2 s. Increasing the decision threshold to $\tau = 0.5$ slightly degrades the RMSE and results in larger azimuth and elevation angle uncertainties with slightly narrower meteoroid velocity uncertainty, compared to $\tau = 0.4$.

The applied PSO method for reconstructing the trajectory uses 3-D ray tracing with infraGA (Blom, 2014). By applying infraGA, we can incorporate complex ground-to-space atmosphere models (Hetzer, 2024) that include wind to model the acoustic wave propagation in a heterogeneous moving atmosphere. The modelling results in Fig. 6 illustrate that high-quality PN picks provide robust constraints. In addition, slight manual curation of onset picking can improve trajectory fits at present SNR and model training levels. For truly independent and automatic picking without further manual inspection, we suspect that SMORD must be expanded with more training data. Nevertheless, SMORD and the trained PN picker can already be used during manual phase picking as a tool to easily identify seismo-acoustic onsets in waveforms and, thereby, help to quickly find a trajectory and possible strewn field.

6 Discussion

SMORD provides a valuable opportunity for future studies on meteoroids and other seismo-acoustic phenomena. Still, there are only few systematic studies on meteoroid falls observed with seismic networks (e.g., Edwards et al., 2007; Neidhart et al., 2021). None of these previous studies provide easy access to the original waveforms which are necessary to repeat earlier findings or to test new methods and compare their outcome with previous results.

Our data compilation of meteoroid falls, whose

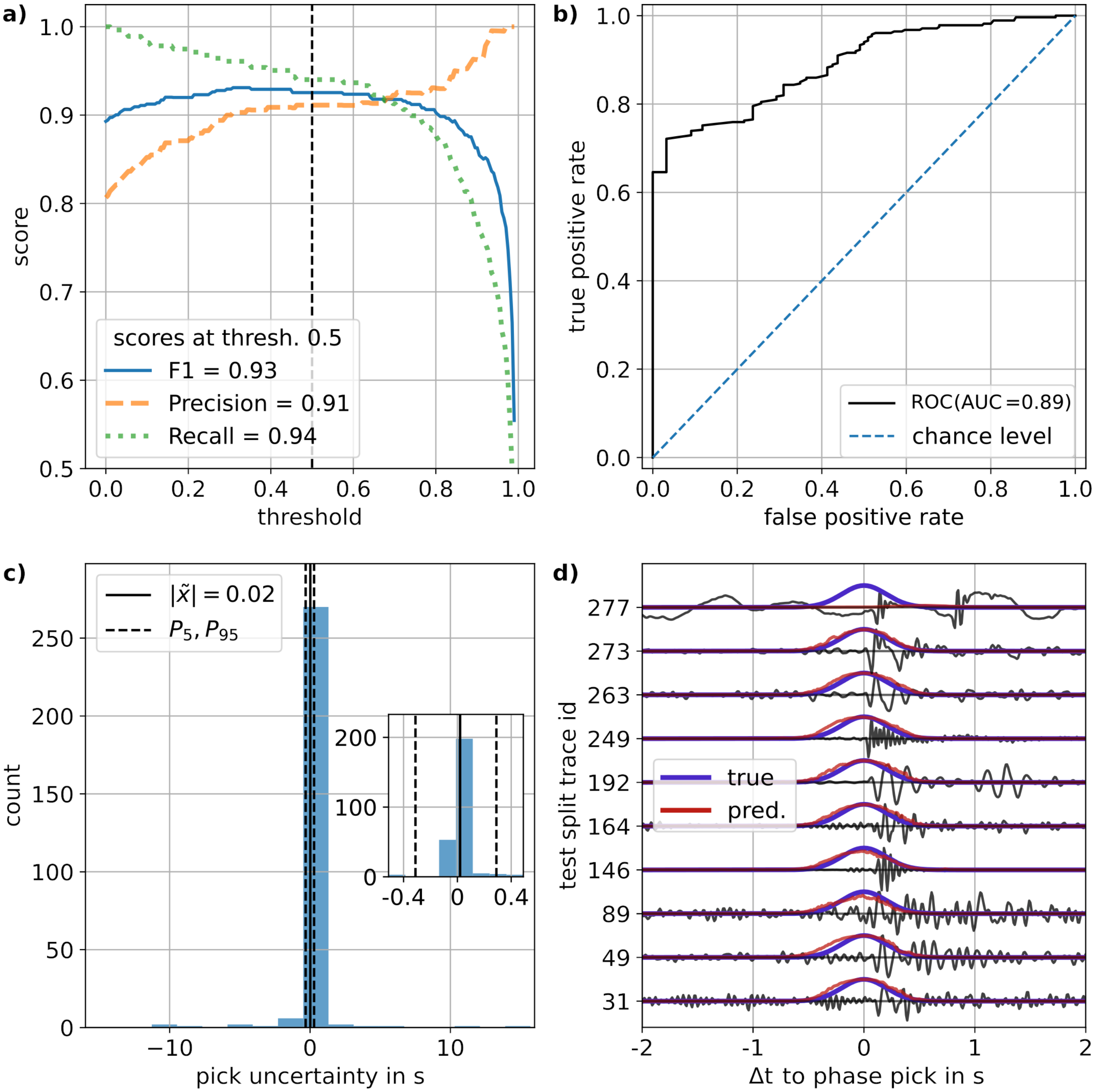

Figure 4 Training results. a) Precision (orange), Recall (green), and F1 (blue) scores versus the decision threshold at which predicted picks are counted as successful hits. The threshold of 0.5 is chosen on the development split. b) Receiver-operating characteristic plot. True positive versus false positive rate of the PN picker (ROC: black line) measures the overall success of the phase pick probability predictions. The AUC value of 0.89 indicates the overall goodness of the fit independent of the chosen decision threshold. A true random picker would predict at equally true and false positive rates, breaking down the success of phase pick predictions to a chance level (50 per cent). This is shown here as the blue dashed diagonal. c) Histogram of the pick uncertainty in seconds versus the time accuracy of the trained PN picker. The median absolute pick uncertainty value is 0.02 s and 90 per cent of pick uncertainty values are found between P_5 = -0.31 s and P_{95} = 0.29 s. The inset histogram shows a zoomed in portion around P_5 and P_{95} with thinner bars. d) Section plot of normalized vertical component seismic traces of the test split arranged by their test split trace id shifted so that $t = 0$ is at the time of the phase pick. The true picks after applying the Gaussian window and the predicted phase pick probabilities are given in blue and red, respectively. Note the overall good match between truths and predictions, but also how the PN picker failed to identify the phase for trace id 277.

seismo-acoustic signals were observed by seismic stations, is unique worldwide. Thereby SMORD will make it easier to study meteoroid properties in detail such as trajectory determinations (e.g., Vida, 2023), energy and mass estimations, or ablation parameters (e.g., Campbell-Brown et al., 2013). For larger objects, the trajectory can be used for refined strewn field mapping before going into the field to search for precious extrater-

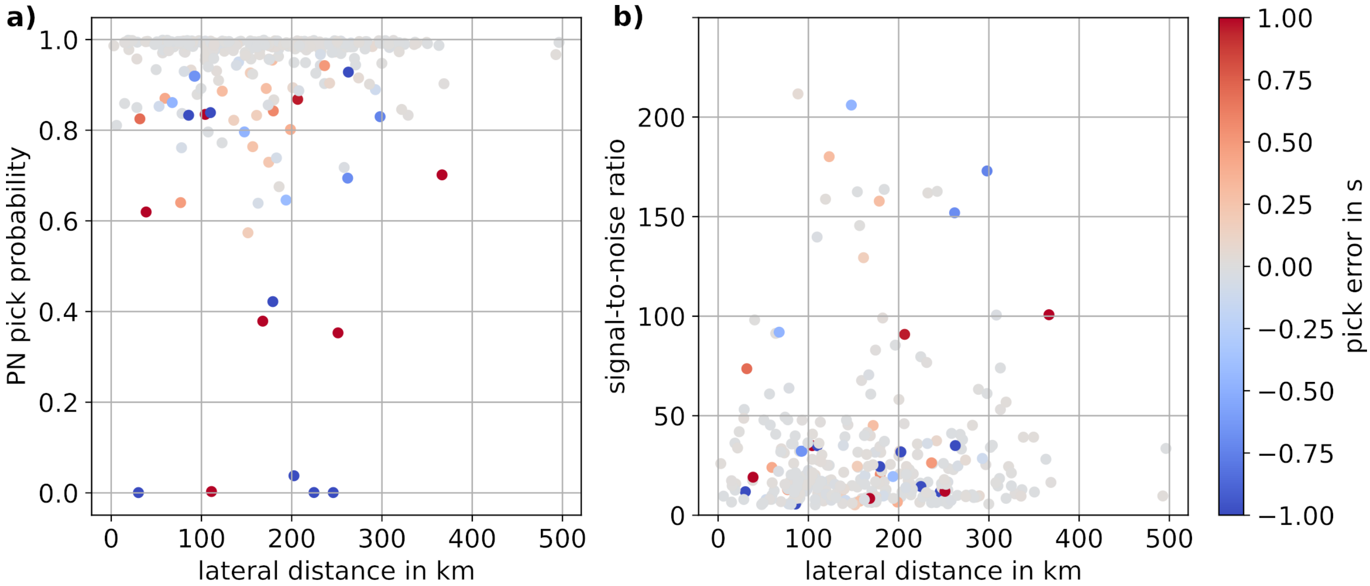

Figure 5 a) Distribution of PN pick probabilities versus lateral distance to the respective meteoroid trajectory midpoint. Color indicates the picking uncertainty of any given PN pick. b) Distribution of SNR of picked phases versus lateral distance and associated PN pick uncertainty.

restrial material.

The search for meteoroid-related seismo-acoustic signals can be quite difficult, because the recorded amplitude depends on numerous factors: source strength, distance or geometrical spreading, atmospheric winds and temperature and frequency-dependent attenuation, background noise, site effects, etc. Due to low SNRs, such signals are often not identified. Another point is that the moveout of seismo-acoustic waves is quite different from earthquake waves, and therefore, seismic data analysts often fail to recognize such waves crossing a seismic network. These issues can be treated with SMORD and our first trained PhaseNet based phase picker to automatically identify meteoroid-induced seismo-acoustic signals. PhaseNet was successfully trained on a global dataset containing a wide variety of seismic sensors at different sites (achieving >90% precision and recall at a decision threshold level of 0.5). This achievement streamlines the process of phase identification when the trained PN picker is used as a tool to aid manual picking routines.

The common approach of training PhaseNet for a specific network is not possible in our case, because there are not enough observations per network. However, we find that the PN picker performs well for meteoroid-related signals with different frequency contents, regardless of specific sites (Fig. 4d). In our application, the PN predictions can be followed over a distance range of up to approximately 250 km to the FRIPON meteoroid trajectory (see Figs. 6g, 6h). This aligns well with the distance ranges we encountered during the compilation of SMORD (see Figs. 1a, 1b, 5a, 5b). We find that the capability to identify seismo-acoustic arrivals largely depends on the source characteristics, recording conditions, and atmospheric conditions.

Uncertainties related to the PN picks are well below the accuracy required for precise trajectory reconstruction. At a decision level of 0.5, 90% of picks are within ± 0.3 s. Together with an acoustic wave velocity of c. 330 m/s this corresponds to a distance uncertainty of just ± 100 m. Here, we note that these pick timing uncertainties are negligible compared to modelling uncertainties due to wind effects on sound propagation or modelling limits such as spatial discretization for wavefield modelling. Meteoroid event trajectories and velocities from existing meteoroid catalogs contain uncertainties; CNEOS records depend on sensor characteristics and processing whereas IMO eyewitness reconstructions are biased towards populated regions and wake-sleep cycles. Thus, their combination is helpful for narrowing down uncertainties. Our manual labeling during the initial phase identification of SMORD may omit weak or ambiguous arrivals and inter-analyst variability remains but can be mitigated by guidelines. Atmospheric state variability (winds and temperature stratification) was not modeled explicitly during the initial phase identification of the seismo-acoustic onsets and likely explains some false detections of the PN picker.

A major future application could be autonomous, continuous monitoring, detection, and localization of meteoroid falls using seismic data. The 4-step workflow we presented can be automated almost completely and the only user input would be origin time and location, which would allow for a rapid meteoroid trajectory calculation. The observational basis, which is continuous online waveform data, already exists in many continental regions due to open data centers such as EIDA (Strollo et al., 2021) or IRIS (Trabant et al., 2012). An extension of these observational capabilities can be expected for the future based on previous experience. Of course, detectors need to be improved to account for wavefields with acoustic moveout, but such issues can be solved and coincidence detection with acoustic moveouts is possible in principle. One feature

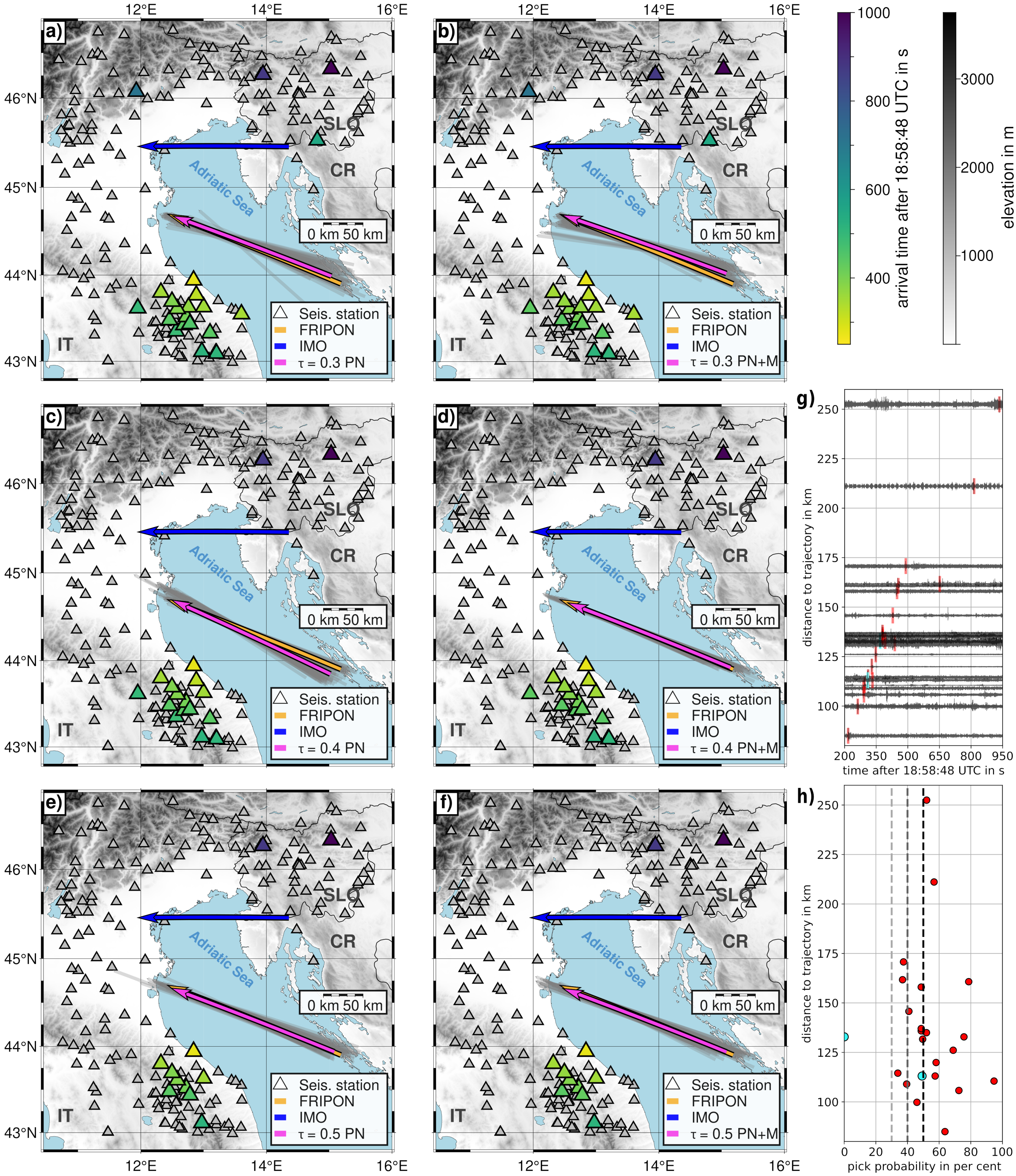

Figure 6 Fireball event on 12th April 2025 across the Adriatic Sea. a-f) FRIPON camera trajectory (yellow arrow) and IMO observation report trajectory (blue arrow). Gray lines show 100 bootstrapped runs, and the median seismic PSO solution trajectory is given as a purple arrow. Seismic station distribution as triangles, colored with respect to the identified arrival time. Gray triangles mark stations that were discarded during PSO modeling, because they do not contain a seismic onset surpassing the given pick decision threshold. a, c, e) show the distribution of used stations, bootstrapped PSO runs and median PSO solution for case 1 (no manual correction, see text) with pick decision thresholds τ of 0.3, 0.4, and 0.5, respectively. b, d, f) same as a, c, e), but for case 2 with PN picks manually verified and two corrected PN picks. g) Section plot of the seismic waveforms: Red bars show the onsets of the PN picks and blue bars show the two manually corrected picks. h) Pick probability versus distance to the trajectory midpoint. Red circles mark the PN pick probabilities, and blue circles mark the pick probabilities at the manually set pick. The probability at one of the manually set picks is 0, meaning the PN picker failed to identify the phase. The pick decision thresholds 0.3, 0.4, 0.5 are drawn as dashed gray to black lines.

Trajectory source	Median azimuth angle in °	Median elevation angle in °	Median velocity in km/s	Median RMSE in s
IMO Event 2077-2025	270.9	-	-	-
FRIPON Event 24644	292.9	12.1	26.3	-
PSO solution τ = 0.3 PN (21 picks, case 1)	290.6 ± 4.5	13.6 ± 2.7	24.4 ± 2.5	26.9
PSO solution τ = 0.3 PN (21 picks, case 2)	288.6 ± 5.3	12.8 ± 3.5	26.1 ± 2.6	18.5
PSO solution τ = 0.4 PN (17 picks, case 1)	294.9 ± 5.1	12.8 ± 1.2	26.6 ± 2.5	18.0
PSO solution τ = 0.4 PN (17 picks, case 2)	291.6 ± 1.8	12.8 ± 0.9	26.4 ± 3.9	2.2
PSO solution τ = 0.5 PN (11 picks, case 1)	291.2 ± 2.4	12.4 ± 1.7	26.4 ± 2.9	10.8
PSO solution τ = 0.5 PN (11 picks, case 2)	291.1 ± 2	12.7 ± 1.7	26.4 ± 2.3	2.7

Table 4 Comparison of FRIPON trajectory parameters with automatic PSO solutions (case 1) and with corrected data (case 2 with two manual pick corrections). Trajectory uncertainties are calculated from the 90 percent confidence interval of the 100 PSO solutions. The RMSE is the misfit between modelled and observed arrival times and the median RMSE is the misfit over all 100 PSO trajectories.

which could be used is the addition of the typical waveform pattern, associated with meteoroid related onsets, which is W-shaped on the vertical component in the beginning of the wavetrain with a downward motion due to the downward propagating pressure front (Kanamori et al., 1991; Edwards et al., 2008). This enhanced detection approach would be especially valuable for detecting meteoroids during the daytime, when optical methods struggle due to the daytime light conditions which lead to oversaturation of the cameras. Another crucial application would be signal detection during the dark flight phase at the end of the trajectory which is important for estimating strewn fields (Devillepoix et al., 2018; Moilanen et al., 2021).

Another possible future application of SMORD is the evaluation of site effects and local coupling effects at seismological recording stations. Shallow geological features as well as above surface features such as buildings or steep topography affect the efficiency with which the acoustic wave can couple into the subsurface and convert into seismic waves. Depending on the local geology, seismo-acoustic wave amplitudes might be dampened or amplified and the waveform clarity can be affected by the site effects as well (Edwards et al., 2008; Novoselov et al., 2020). In a future application the measurement of seismic amplitudes and their comparison with amplitudes from acoustic infrasound measurements can be used to better estimate seismo-acoustic coupling coefficients (Novoselov et al., 2020; Bishop et al., 2022), because amplitude information helps to determine the energy or mass of a supersonic object (e.g., Edwards et al., 2007). As there are many more seismic stations than infrasound sensors available for scientific and forensic studies, seismological analysis will enable better investigations of events with strong acoustic emissions, e.g., accidental explosions (Hinzen, 2007) or combat actions (Dando et al., 2023).

7 Conclusions

We introduce SMORD, a curated dataset of 3,295 seismo-acoustic picks from 316 meteoroid events and demonstrate that a PhaseNet model, trained on SMORD labels, can detect meteoroid air-to-ground coupled seismic waves with >90% precision and recall on a test subset of events. SMORD and the associated phase-identification model provide a reproducible foundation for automated meteor signal detection in seismic data and for multimodal bolide analyses.

The trained picker enables rapid scanning of regional seismic archives following reported bolides, supporting time-critical meteorite searches and initial trajectory inference. Integration with GLM detections (Jenniskens et al., 2018), with radar (CMOR/BRAMS), and with infrasound arrays will enable joint constraints on source time-height functions and energy deposition. As GLM and global seismic recording coverage continue to grow, SMORD-like labels can power near real-time pipelines.

Future work will focus on integrating atmospheric propagation modeling with the automatic identification of seismo-acoustic arrivals. Coupling the current workflow with atmospheric propagation models (e.g., ray tracing with infraGA (Blom, 2014), constrained by reanalysis wind fields (Hetzer, 2024) is expected to improve the physical consistency of predicted travel times and phase associations. Additionally, we plan to expand the compiled database by lowering the thresholds of 100 IMO sightings and the 0.3 kt CNEOS yields, as well as incorporating additional meteoroid observations from external networks, such as FRIPON (Colas et al., 2020) and the Global Meteor Network (GMN) (Vida et al., 2021). This will increase the number and diversity of events available for training and validation. Regarding machine learning, we will investigate training strategies dedicated to infrasound data. This will include separate models for array-based recordings and individual stations to better capture differences in waveform characteristics and noise conditions. Finally, we will explore joint seismic-acoustic phase identification to leverage complementary information from ground motion and pressure waveforms, aiming to improve robustness and reduce picking ambiguities.

Acknowledgements

We thank data providers and network operators who shared seismic data via FDSN services, as well as the International Meteor Organization and NASA CNEOS for public meteor catalogs. We appreciate community tools including InfraGA, PySwarms, NCPAG2S-CLC, ObsPy, SeisBench and PyGMT.

We thank Janis Heuel for helping with the initial setup of the SeisBench and PhaseNet training and sharing practical tips on data preparation and training setup.

This work was supported by funding from the Vector Stiftung project "SeisMET – Seismologische Detektion von Meteoren".

We thank the editor Kenneth Macpherson, reviewer C. Pilger and an anonymous reviewer for constructive reviews which clarified several issues in the manuscript.

Data and code availability

The dataset containing the SMORD metadata and picks, as well as the exact training/validation/test splits, and the model code and weights, are openly available in the Zenodo repository at 10.5281/zenodo.20827548. FDSN-Network references can be found in the Appendix.

Competing Interests

The authors declare no competing interests.

References

Andrioli, V. F., Fritts, D. C., Batista, P. P., and Clemesha, B. R. Improved analysis of all-sky meteor radar measurements of gravity wave variances and momentum fluxes. *Annales Geophysicae*, 31(5):889–908, May 2013. doi: 10.5194/angeo-31-889-2013.

Arrowsmith, S. J., Drob, D. P., Hedlin, M. A. H., and Edwards, W. A joint seismic and acoustic study of the Washington State bolide: Observations and modeling. *Journal of Geophysical Research: Atmospheres*, 112(D9), May 2007. doi: 10.1029/2006jd008001.

Beyreuther, M., Barsch, R., Krischer, L., Megies, T., Behr, Y., and Wassermann, J. ObsPy: A Python Toolbox for Seismology. *Seismological Research Letters*, 81(3):530–533, May 2010. doi: 10.1785/gssrl.81.3.530.

Bishop, J. W., Fee, D., Modrak, R., Tape, C., and Kim, K. Spectral Element Modeling of Acoustic to Seismic Coupling Over Topography. *Journal of Geophysical Research: Solid Earth*, 127(1), Jan. 2022. doi: 10.1029/2021jb023142.

Blom, P. Infraga/geoac, 2014. https://github.com/LANL-Seismoacoustics/infraGA. Last viewed October 19, 2025).

Blom, P., Gammans, C., Delbridge, B., and Carmichael, J. D. Prediction of regional infrasound produced by supersonic sources using a ray-based Mach cone source. *The Journal of the Acoustical Society of America*, 155(3):1667–1681, Mar. 2024. doi: 10.1121/10.0025025.

Bridle, J. S. *Probabilistic Interpretation of Feedforward Classification Network Outputs, with Relationships to Statistical Pattern Recognition*, page 227–236. Springer Berlin Heidelberg, 1990. doi: 10.1007/978-3-642-76153-9_28.

Brown, P., Edwards, W., ReVelle, D., and Spurny, P. Acoustic analysis of shock production by very high-altitude meteors—I: infrasonic observations, dynamics and luminosity. *Journal of Atmospheric and Solar-Terrestrial Physics*, 69(4-5):600–620, Apr. 2007. doi: 10.1016/j.jastp.2006.10.011.

Buda, M., Maki, A., and Mazurowski, M. A. A systematic study of the class imbalance problem in convolutional neural networks. *Neural Networks*, 106:249–259, Oct. 2018. doi: 10.1016/j.neunet.2018.07.011.

Campbell-Brown, M. D., Borovička, J., Brown, P. G., and Stokan, E. High-resolution modelling of meteoroid ablation. *Astronomy & Astrophysics*, 557:A41, Aug. 2013. doi: 10.1051/0004-6361/201322005.

Ceplecha, Z., Borovička, J., Elford, W. G., ReVelle, D. O., Hawkes, R. L., Porubčan, V., and Šimek, M. Meteor Phenomena and Bodies. *Space Science Reviews*, 84(3-4), 1998. doi: 10.1023/a:1005069928850.

Colas, F., Zanda, B., Bouley, S., Jeanne, S., Malgoyre, A., Birlan, M., Blanpain, C., Gattacceca, J., Jorda, L., Lecubin, J., Marmo, C., Rault, J. L., Vaubaillon, J., Vernazza, P., Yohia, C., Gardiol, D., Nedelcu, A., Poppe, B., Rowe, J., Forcier, M., Koschny, D., Trigo-Rodriguez, J. M., Lamy, H., Behrend, R., Ferrière, L., Barghini, D., Buzzoni, A., Carbognani, A., Di Carlo, M., Di Martino, M., Knapic, C., Londero, E., Pratesi, G., Rasetti, S., Riva, W., Stirpe, G. M., Valsecchi, G. B., Volpicelli, C. A., Zorba, S., Coward, D., Drolshagen, E., Drolshagen, G., Hernandez, O., Jehin, E., Jobin, M., King, A., Nitschelm, C., Ott, T., Sanchez-Lavega, A., Toni, A., Abraham, P., Affaticati, F., Albani, M., Andreis, A., Andrieu, T., Anghel, S., Antaluca, E., Antier, K., Appéré, T., Armand, A., Ascione, G., Audureau, Y., Auxepaules, G., Avoscan, T., Baba Aissa, D., Bacci, P., Bădescu, O., Baldini, R., Baldo, R., Balestrero, A., Baratoux, D., Barbotin, E., Bardy, M., Basso, S., Bautista, O., Bayle, L. D., Beck, P., Bellitto, R., Belluso, R., Benna, C., Benammi, M., Beneteau, E., Benkhaldoun, Z., Bergamini, P., Bernardi, F., Bertaina, M. E., Bessin, P., Betti, L., Bettonvil, F., Bihel, D., Birnbaum, C., Blagoi, O., Blouri, E., Boacă, I., Boată, R., Bobiet, B., Bonino, R., Boros, K., Bouchet, E., Borgeot, V., Bouchez, E., Boust, D., Boudon, V., Bouman, T., Bourget, P., Brandenburg, S., Bramond, P., Braun, E., Bussi, A., Cacault, P., Caillier, B., Calegaro, A., Camargo, J., Caminade, S., Campana, A. P. C., Campbell-Burns, P., Canal-Domingo, R., Carell, O., Carreau, S., Cascone, E., Cattaneo, C., Cauhape, P., Cavier, P., Celestin, S., Cellino, A., Champenois, M., Chennaoui Aoudjehane, H., Chevrier, S., Cholvy, P., Chomier, L., Christou, A., Cricchio, D., Coadou, P., Cocaign, J. Y., Cochard, F., Cointin, S., Colombi, E., Colque Saavedra, J. P., Corp, L., Costa, M., Costard, F., Cottier, M., Cournoyer, P., Coustal, E., Cremonese, G., Cristea, O., Cuzon, J. C., D'Agostino, G., Daiffallah, K., Dănescu, C., Dardon, A., Dasse, T., Davadan, C., Debs, V., Defaix, J. P., Deleflie, F., D'Elia, M., De Luca, P., De Maria, P., Deverchère, P., Devillepoix, H., Dias, A., Di Dato, A., Di Luca, R., Dominici, F. M., Drouard, A., Dumont, J. L., Dupouy, P., Duvignac, L., Egal, A., Erasmus, N., Esseiva, N., Ebel, A., Eisengarten, B., Federici, F., Feral, S., Ferrant, G., Ferreol, E., Finitzer, P., Foucault, A., Francois, P., Frîncu, M., Froger, J. L., Gaborit, F., Gagliarducci, V., Galard, J., Gardavot, A., Garmier, M., Garnung, M., Gautier, B., Gendre, B., Gerard, D., Gerardi, A., Godet, J. P., Grandchamps, A., Grouiez, B., Groult, S., Guidetti, D., Giuli, G., Hello, Y., Henry, X., Herbreteau, G., Herpin, M., Hewins, P., Hillairet, J. J., Horak, J., Hueso, R., Huet, E., Huet, S., Hyaumé, F., Interrante, G., Isselin, Y., Jeangeorges, Y., Janeux, P., Jeanneret, P., Jobse, K., Jouin, S., Jouvard, J. M., Joy, K., Julien, J. F., Kacerek, R., Kaire, M., Kempf, M., Koschny, D., Krier, C., Kwon, M. K., Lacassagne, L., Lachat, D., Lagain, A., Laisné, E., Lanchares, V., Laskar, J., Lazzarin, M., Leblanc, M., Lebreton, J. P., Lecomte, J., Le Dû, P., Lelong, F., Lera, S., Leoni, J. F., Le-Pichon, A., Le-Poupon, P., Leroy, A., Leto, G., Levansuu, A., Lewin, E., Lienard, A., Licchelli, D., Locatelli, H., Loehle, S., Loizeau, D., Luciani, L., Maignan, M., Manca, F., Mancuso, S., Mandon, E., Mangold, N., Mannucci, F., Maquet, L., Marant, D., Marchal, Y., Marin, J. L., Martin-Brisset, J. C., Martin, D., Mathieu, D., Maury, A., Mespoulet, N., Meyer, F., Meyer, J. Y., Meza, E., Moggi Cecchi, V., Moiroud, J. J., Millan, M., Montesarchio, M., Misiano, A., Molinari, E., Molau, S., Monari, J., Monflier, B., Monkos, A., Montemaggi, M., Monti, G., Moreau, R., Morin, J., Mourgues, R., Mousis, O., Nablanc, C., Nastasi, A., Niacşu, L., Notez, P., Ory, M., Pace, E., Paganelli, M. A., Pagola, A., Pajuelo, M., Palacián, J. F., Pallier, G., Paraschiv, P., Pardini, R., Pavone, M., Pavy, G., Payen, G., Pegoraro, A., Peña-Asensio, E., Perez, L., Pérez-Hoyos, S., Perlerin, V., Peyrot, A., Peth, F., Pic, V., Pietronave, S., Pilger, C., Piquel, M., Pisanu, T., Poppe, M., Portois, L., Prezeau, J. F., Pugno, N., Quantin, C., Quitté, G., Rambaux, N., Ravier, E., Repetti, U., Ribas, S., Richard, C., Richard, D., Rigoni, M., Rivet, J. P., Rizzi, N., Rochain, S., Rojas, J., Romeo, M., Rotaru, M., Rotger, M., Rougier, P., Rousselot, P., Rousset, J., Rousseu, D., Rubiera, O., Rudawska, R., Rudelle, J., Ruguet, J., Russo, P., Sales, S., Sauzereau, O., Salvati, F., Schieffer, M., Schreiner, D., Scribano, Y., Selvestrel, D., Serra, R., Shengold, L., Shuttleworth, A., Smareglia, R., Sohy, S., Soldi, M., Stanga, R., Steinhausser, A., Strafella, F., Sylla Mbaye, S., Smedley, A. R. D., Tagger, M., Tanga, P., Taricco, C., Teng, J. P., Tercu, J. O., Thizy, O., Thomas, J. P., Tombelli, M., Trangosi, R., Tregon, B., Trivero, P., Tukkers, A., Turcu, V., Umbriaco, G., Unda-Sanzana, E., Vairetti, R., Valenzuela, M., Valente, G., Varennes, G., Vauclair, S., Vergne, J., Verlinden, M., Vidal-Alaiz, M., Vieira-Martins, R., Viel, A., Vîntdevară, D. C., Vinogradoff, V., Volpini, P., Wendling, M., Wilhelm, P., Wohlgemuth, K., Yanguas, P., Zagarella, R., and Zollo, A. FRIPON: a worldwide network to track incoming meteoroids. *Astronomy & Astrophysics*, 644:A53, Dec. 2020. doi: 10.1051/0004-6361/202038649.

Dando, B. D. E., Goertz-Allmann, B. P., Brissaud, Q., Köhler, A., Schweitzer, J., Kværna, T., and Liashchuk, A. Identifying attacks in the Russia–Ukraine conflict using seismic array data. *Nature*, 621(7980):767–772, Aug. 2023. doi: 10.1038/s41586-023-06416-7.

Devillepoix, H. A. R., Sansom, E. K., Bland, P. A., Towner, M. C., Cupák, M., Howie, R. M., Jansen-Sturgeon, T., Cox, M. A., Hartig, B. A. D., Benedix, G. K., and Paxman, J. P. The Dingle Dell meteorite: A Halloween treat from the Main Belt. *Meteoritics & Planetary Science*, 53(10), 2018. doi: 10.1111/maps.13142.

Drolshagen, G., Koschny, D., Drolshagen, S., Kretschmer, J., and Poppe, B. Mass accumulation of earth from interplanetary dust, meteoroids, asteroids and comets. *Planetary and Space Science*, 143, 2017. doi: 10.1016/j.pss.2016.12.010.

Edwards, W. N., Eaton, D. W., McCausland, P. J., ReVelle, D. O., and Brown, P. G. Calibrating infrasonic to seismic coupling using the Stardust sample return capsule shockwave: Implications for seismic observations of meteors. *Journal of Geophysical Research: Solid Earth*, 112(B10), Oct. 2007. doi: 10.1029/2006jb004621.

Edwards, W. N., Eaton, D. W., and Brown, P. G. Seismic observations of meteors: Coupling theory and observations. *Reviews of Geophysics*, 46(4), Dec. 2008. doi: 10.1029/2007rg000253.

Ens, T., Brown, P., Edwards, W., and Silber, E. Infrasound production by bolides: A global statistical study. *Journal of Atmospheric and Solar-Terrestrial Physics*, 80:208–229, May 2012. doi: 10.1016/j.jastp.2012.01.018.

Fernando, B. and Charalambous, C. Reentry and disintegration dynamics of space debris tracked using seismic data. *Science*, 391 (6783):412–416, Jan. 2026. doi: 10.1126/science.adz4676.

Fernando, B., Charalambous, C., Saliby, C., Sansom, E., Larmat, C., Buttsworth, D., Hicks, D., Johnson, R., Lewis, K., McCleary, M., Petricca, G., Schmerr, N., Zander, F., and Inman, J. Seismoacoustic measurements of the OSIRIS-REx re-entry with an off-grid Raspberry PiShake. *Seismica*, 3(1), Mar. 2024. doi: 10.26443/seismica.v3i1.1154.

Fireball Recovery and InterPlanetary Observation Nework. Multiple event 2025-04-12 18:58:46 UTC, 2025. https://fireball.fripon.org/displaymultiple.php?id=24664. Accessed from.

Gritsevich, M. Determination of parameters of meteor bodies based on flight observational data. *Advances in Space Research*, 44(3):323–334, Aug. 2009. doi: 10.1016/j.asr.2009.03.030.

Hankey, M. and Perlerin, V. IMO Fireball Reports. In *Proceedings of the International Meteor Conference*, page 160, Giron, France, 2014. International Meteor Organization.

Hetzer, C. The NCPAG2S Command-Line Client [software], 2024. doi: 10.5281/zenodo.13345069.

Hinzen, K.-G. London Fuel Tank Explosion Recorded by Short-period Seismic Stations at 500-km Distance. *Seismological Research Letters*, 78(3):383–388, May 2007. doi: 10.1785/gssrl.78.3.383.

International Meteor Organization. Fireball Events Browser, 2025a. https://fireball.imo.net/members/imo_view/browse_events. Accessed 2025-10-19.

International Meteor Organization. Fireball Event 2077-2025, 2025b. https://fireballs.imo.net/members/imo_view/event/2025/2077. Accessed 2025-12-15.

Jenniskens, P., Albers, J., Tillier, C. E., Edgington, S. F., Longenbaugh, R. S., Goodman, S. J., Rudlosky, S. D., Hildebrand, A. R., Hanton, L., Ciceri, F., Nowell, R., Lyytinen, E., Hladiuk, D., Free, D., Moskovitz, N., Bright, L., Johnston, C. O., and Stern, E. Detection of meteoroid impacts by the Geostationary Lightning Mapper on the GOES-16 satellite. *Meteoritics & Planetary Science*, 53 (12), 2018. doi: 10.1111/maps.13137.

Jones, J., Brown, P., Ellis, K., Webster, A., Campbell-Brown, M., Krzemenski, Z., and Weryk, R. The Canadian Meteor Orbit Radar: system overview and preliminary results. *Planetary and Space Science*, 53(4):413–421, Apr. 2005. doi: 10.1016/j.pss.2004.11.002.

Kanamori, H., Mori, J., Anderson, D. L., and Heaton, T. H. Seismic excitation by the space shuttle Columbia. *Nature*, 349(6312): 781–782, Feb. 1991. doi: 10.1038/349781a0.

Kennedy, J. and Eberhart, R. Particle swarm optimization. In *Proceedings of ICNN'95 - International Conference on Neural Networks*, volume 4 of *ICNN-95*, page 1942–1948. IEEE, 1995. doi: 10.1109/icnn.1995.488968.

Koschny, D. and Borovicka, J. Definitions of terms in meteor astronomy. *WGN, Journal of the International Meteor Organization*, 45(5):91–92, 2017.

Lamy, H., Verbeeck, C., Balis, J., Anciaux, M., and Calders, S. Observability Function of the BRAMS Meteor Radio Forward Scatter Network. In *Asteroids, Comets, Meteors Conference*, volume 2851, page 2134, 2023. https://www.hou.usra.edu/meetings/acm2023/pdf/2134.pdf.

Loshchilov, I. and Hutter, F. SGDR: Stochastic Gradient Descent with Warm Restarts, 2016. doi: 10.48550/ARXIV.1608.03983.

Loshchilov, I. and Hutter, F. Decoupled Weight Decay Regularization, 2017. doi: 10.48550/ARXIV.1711.05101.

Miranda, L. PySwarms: a research toolkit for Particle Swarm Optimization in Python. *Journal of Open Source Software*, 3(21),

2018. doi: 10.21105/joss.00433.

Moilanen, J., Gritsevich, M., and Lyytinen, E. Determination of strewn fields for meteorite falls. *Monthly Notices of the Royal Astronomical Society*, 503(3):3337–3350, Mar. 2021. doi: 10.1093/mnras/stab586.

Moorhead, A., Cooke, B., Blaauw, R., Moser, D., and Ehlert, S. A Meteoroid Handbook for Aerospace Engineers and Managers, 2019. No. NASA/TM-2019-220142).

Münchmeyer, J. and Woollam, J. Welcome to SeisBench, 2025. https://seisbench.readthedocs.io/en/stable/. Retrieved January 14, 2026.

NASA/JPL. NASA/JPL Center for Near-Earth Object Studies (CNEOS), 2025. https://cneos.jpl.nasa.gov/fireballs/. Accessed 2025-10-19.

Neidhart, T., Miljković, K., Sansom, E. K., Devillepoix, H. A. R., Kawamura, T., Dimech, J.-L., Wieczorek, M. A., and Bland, P. A. Statistical analysis of fireballs: Seismic signature survey. *Publications of the Astronomical Society of Australia*, 38, 2021. doi: 10.1017/pasa.2021.11.

Northern California Earthquake Data Center. Northern California Earthquake Data Center, 2014. doi: 10.7932/NCEDC.

Novoselov, A., Fuchs, F., and Bokelmann, G. Acoustic-to-seismic ground coupling: coupling efficiency and inferring near-surface properties. *Geophysical Journal International*, 223(1), 2020. doi: 10.1093/gji/ggaa304.

Ott, T., Drolshagen, E., Koschny, D., Mialle, P., Pilger, C., Vaubaillon, J., Drolshagen, G., and Poppe, B. Combination of infrasound signals and complementary data for the analysis of bright fireballs. *Planetary and Space Science*, 179:104715, Dec. 2019. doi: 10.1016/j.pss.2019.104715.

Pascanu, R., Mikolov, T., and Bengio, Y. On the difficulty of training recurrent neural networks. In *Proceedings of ICML*, page 1310–1318. PMLR, 2013.

Paszke, A., Gross, S., Massa, F., Lerer, A., Bradbury, J., Chanan, G., and Chintala, S. Pytorch: An imperative style, high-performance deep learning library. In *Advances in neural information processing systems*, page 32. 2019.

Pilger, C., Gaebler, P., Hupe, P., Ott, T., and Drolshagen, E. Global Monitoring and Characterization of Infrasound Signatures by Large Fireballs. *Atmosphere*, 11(1):83, Jan. 2020. doi: 10.3390/atmos11010083.

Pujol, J., Rydelek, P., and Bohlen, T. Determination of the Trajectory of a Fireball Using Seismic Network Data. *Bulletin of the Seismological Society of America*, 95(4):1495–1509, Aug. 2005. doi: 10.1785/0120040155.

Raspberry Shake, S. A. Raspberry Shake, 2016. doi: 10.7914/SN/AM.

ReVelle, D. O. On meteor-generated infrasound. *Journal of Geophysical Research*, 81(7):1217–1230, Mar. 1976. doi: 10.1029/ja081i007p01217.

Ringler, A. T., Anthony, R. E., Aster, R. C., Ammon, C. J., Arrowsmith, S., Benz, H., Ebeling, C., Frassetto, A., Kim, W., Koelemeijer, P., Lau, H. C. P., Lekić, V., Montagner, J. P., Richards, P. G., Schaff, D. P., Vallée, M., and Yeck, W. Achievements and Prospects of Global Broadband Seismographic Networks After 30 Years of Continuous Geophysical Observations. *Reviews of Geophysics*, 60(3), 2022. doi: 10.1029/2021rg000749.

Sasse, L., Nicolaisen-Sobesky, E., Dukart, J., Eickhoff, S. B., Götz, M., Hamdan, S., Komeyer, V., Kulkarni, A., Lahnakoski, J. M., Love, B. C., Raimondo, F., and Patil, K. R. Overview of leakage scenarios in supervised machine learning. *Journal of Big Data*, 12(1), May 2025. doi: 10.1186/s40537-025-01193-8.

SCEDC. Southern California Earthquake Data Center, 2013. doi: 10.7909/C3WD3XH1.

Silber, E. A. Perspectives and Challenges in Bolide Infrasound Processing and Interpretation: A Focused Review with Case Studies. *Remote Sensing*, 16(19), 2024. doi: 10.3390/rs16193628.

Silber, E. A. and Bowman, D. C. Along-Trajectory Acoustic Signal Variations Observed During the Hypersonic Re-Entry of the OSIRIS-REx Sample Return Capsule. *Seismological Research Letters*, 96(5):2767–2779, Apr. 2025. doi: 10.1785/0220250014.

Silber, E. A. and Brown, P. G. Optical observations of meteors generating infrasound—I: Acoustic signal identification and phenomenology. *Journal of Atmospheric and Solar-Terrestrial Physics*, 119:116–128, Nov. 2014. doi: 10.1016/j.jastp.2014.07.005.

Silber, E. A., Brown, P. G., and Krzeminski, Z. Optical observations of meteors generating infrasound: Weak shock theory and validation. *Journal of Geophysical Research: Planets*, 120(3): 413–428, Mar. 2015. doi: 10.1002/2014je004680.

Sokolova, M. and Lapalme, G. A systematic analysis of performance measures for classification tasks. *Information Processing & Management*, 45(4), 2009. doi: 10.1016/j.ipm.2009.03.002.

Strollo, A., Cambaz, D., Clinton, J., Danecek, P., Evangelidis, C. P., Marmureanu, A., Ottemöller, L., Pedersen, H., Sleeman, R., Stammler, K., Armbruster, D., Bienkowski, J., Boukouras, K., Evans, P. L., Fares, M., Neagoe, C., Heimers, S., Heinloo, A., Hoffmann, M., Kaestli, P., Lauciani, V., Michalek, J., Odon Muhire, E., Ozer, M., Palangeanu, L., Pardo, C., Quinteros, J., Quintiliani, M., Antonio Jara-Salvador, J., Schaeffer, J., Schloemer, A., and Triantafyllis, N. EIDA: The European Integrated Data Archive and Service Infrastructure within ORFEUS. *Seismological Research Letters*, 92(3):1788–1795, Mar. 2021. doi: 10.1785/0220200413.

Trabant, C., Hutko, A. R., Bahavar, M., Karstens, R., Ahern, T., and Aster, R. Data Products at the IRIS DMC: Stepping Stones for Research and Other Applications. *Seismological Research Letters*, 83(5), 2012. doi: 10.1785/0220120032.

Vera Rodriguez, I., Isken, M. P., Dahm, T., Lamb, O. D., Wu, S.-M., Kristjánsdóttir, S., Jónsdóttir, K., Sanchez-Pastor, P., Clinton, J., Wollin, C., Baird, A. F., Wuestefeld, A., Booz, B., Eibl, E. P. S., Heimann, S., Goertz-Allmann, B. P., Jousset, P., Oye, V., Hjörleifsdóttir, V., and Obermann, A. Acoustic signals of a meteoroid recorded on a large-N seismic network and fiber-optic cables. *Seismological Research Letters*, 94(2A):731–745, Nov. 2022. doi: 10.1785/0220220236.

Vida, D. Estimating Fireball Trajectories Using Seismic and Acoustic Data. *WGN, Journal of the International Meteor Organization*, 51(5):132–140, 2023.

Vida, D., Šegon, D., Gural, P. S., Brown, P. G., McIntyre, M. J. M., Dijkema, T. J., Pavletić, L., Kukić, P., Mazur, M. J., Eschman, P., Roggemans, P., Merlak, A., and Zubović, D. The Global Meteor Network – Methodology and first results. *Monthly Notices of the Royal Astronomical Society*, 506(4):5046–5074, Aug. 2021. doi: 10.1093/mnras/stab2008.

Webster, A. R., Brown, P. G., Jones, J., Ellis, K. J., and Campbell-Brown, M. Canadian Meteor Orbit Radar (CMOR). *Atmospheric Chemistry and Physics*, 4(3):679–684, May 2004. doi: 10.5194/acp-4-679-2004.

Woollam, J., Münchmeyer, J., Tilmann, F., Rietbrock, A., Lange, D., Bornstein, T., Diehl, T., Giunchi, C., Haslinger, F., Jozinović, D., Michelini, A., Saul, J., and Soto, H. SeisBench—A Toolbox for Machine Learning in Seismology. *Seismological Research Letters*, 93(3):1695–1709, Mar. 2022. doi: 10.1785/0220210324.

Zhu, W. and Beroza, G. C. PhaseNet: A Deep-Neural-Network-Based Seismic Arrival Time Picking Method. *Geophysical Journal International*, 2019. doi: 10.1093/gji/ggy423.